PERGAMON

International Journal of Heat and Mass Transfer 42 (1999) 2219–2232

International Journal of HEAT and MASS TRANSFER

A fractal geometry model for evaluating permeabilities of porous preforms used in liquid composite molding

R. Pitchumani*, B. Ramakrishnan

Composites Processing Laboratory, Department of Mechanical Engineering, University of Connecticut, U-139, Storrs, CT 06269-3139, U.S.A.

Received 19 March 1998; in final form 5 August 1998

Abstract

Permeation of a net-shaped porous preform by a catalyzed thermosetting resin is an important step in the fabrication of fiber-reinforced composite materials using liquid molding techniques. Determination of the preform permeabilities is critical for an accurate analysis and design of these processes. The complex labyrinth of the preform pore structures, however, presents a major challenge to a quantitative description of the microstructures, and consequently, the evaluation of their permeabilities. Toward addressing this problem, a fundamental description of the disordered preform pore structures using fractal techniques is presented. A fractal permeation model is developed which relates the preform permeabilities to the actual microstructures in terms of two fractal dimensions—one relating the size of the capillary flow pathways to their population, and the other describing the tortuosity of the capillary pathways. The analytical model predictions are validated by experimentally-determined permeabilities for a wide range of preform and process parameters. The model development, experimental studies and the model validation are presented and discussed. The methodology presented may be extended to analyzing transport through porous media arising in other application areas as well.

Nomenclature

d_T tortuosity fractal dimension
d_N area fractal dimension
g_v, g_q geometric factors based on the shape of the capillary cross section
L length scale [m]
L_c tortuous length of a capillary [m]
L_o size of a representative cubic volume [m]
$M(L)$ measure of an object with a length scale L
$N(\lambda)$ number of pores of size λ
p_{inj} injection pressure [psi]
$q(\lambda)$ flow rate through a single λ-sized capillary [m^3/s]
Q total flow rate through the preform [m^3/s]
v_f fiber volume fraction in the preform.

Greek symbols
α ratio of the smallest pore size to the largest pore size, $\lambda_{\min}/\lambda_{\max}$
β ratio of largest pore size, $\lambda_{\max}$ to the size of a representative pore volume, L_o
κ principal preform permeability [m^2]
λ size of a pore [m]
$\lambda_{\max}$ size of the largest pore [m].

1. Introduction

Liquid composite molding, including techniques such as resin transfer molding and its variants, offers potential for affordable fabrication of high-performance composite products of complex shapes and sizes [1–3], and is being explored actively for commercial fabrication in diverse applications. The basic steps in a liquid composite molding process, exemplified by resin transfer molding, are

* Corresponding author. Tel.: +1 860 486 0683; fax: +1 860 486 5088; e-mail: pitchu@engr.uconn.edu

0017-9310/99/$ - see front matter
PII: S0017-9310(98)00261-0

shown schematically in Fig. 1(a). The process begins with the stacking of fibrous reinforcement units to obtain a porous net-shaped structure termed a preform. The preform is placed into a closed mold cavity, and subsequently infiltrated by injecting a reactive thermosetting resin into the mold. The resin-saturated preform is then exposed to high temperatures which initiate and sustain a cross-linking polymerization reaction (referred to as the cure of the resin) and transforms the fiber–resin mixture in the mold cavity to a structurally hard composite product. The physical phenomena involved in the process are the fluid mechanics of the resin permeating the preform, and the heat transfer associated with curing of the composite. The two phenomena are in turn influenced by the kinetics and rheological characteristics of the thermosetting resin.

An important—and challenging—problem in the analysis and practical design of liquid molding process is the description of the flow of the resin in the porous

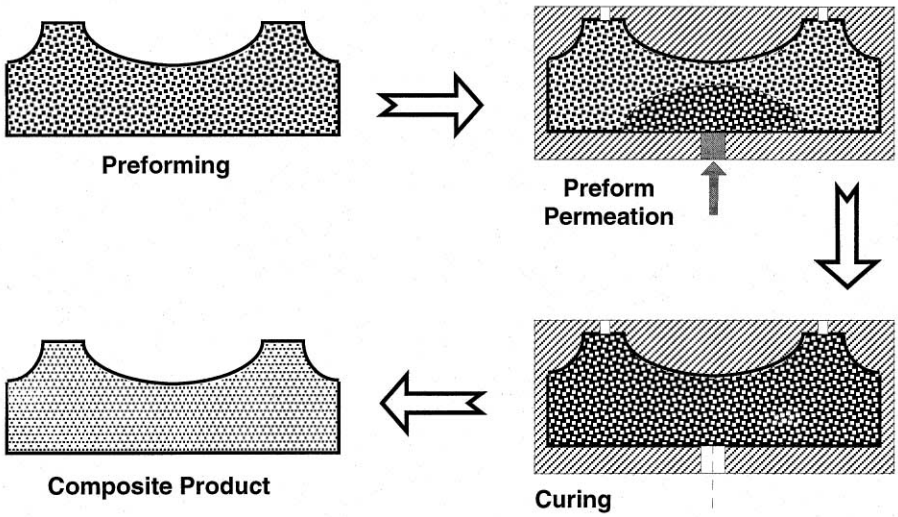

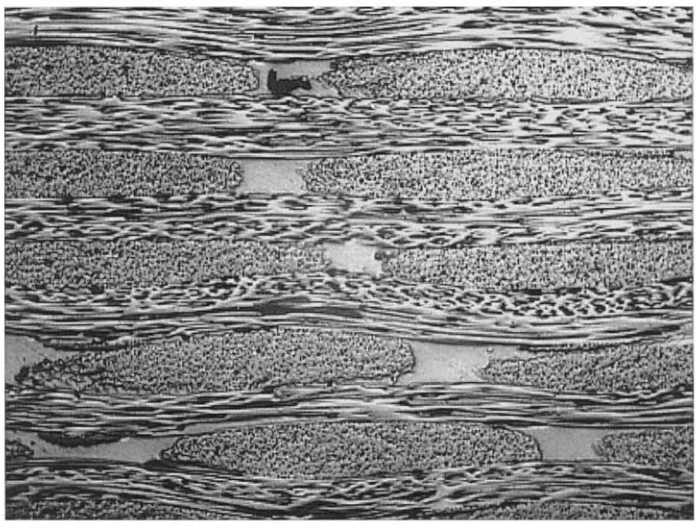

Fig. 1. (a) Schematic of the steps involved in the liquid composite molding process, and (b) microstructure of a resin transfer molded glass–epoxy composite illustrating the disordered pore structure in preforms.

preform. A thorough understanding of the flow behavior is essential for properly designing molds, locating and sizing injection ports and vents, designing injection pressures for complete permeation, and determining mold fill times. Toward this end, several theoretical and experimental investigations have been reported in the literature [4–14]. A common thread weaving all the theoretical approaches is the use of Darcy's law [15, 16] to relate the fluid flow to the pressure gradient, using the fluid viscosity and the permeability of the porous medium.

A key parameter in the Darcian flow description is the preform permeability which is a function of the complex preform pore structure and the fiber volume fraction in the preform. The theoretical derivations of the effective preform permeabilities follow one of two approaches. One approach uses a capillary model with or without a correction factor to account for the effect of capillary tortuosity on the pressure gradient [3, 17] while another approach analyzes flow past a bank of cylinders to arrive at the effective permeabilities [4, 18, 19]. These theoretical approaches, however, model the preform microstructure using idealized arrangements of fibrils and fiber bundles, which are far removed from the actual microstructures such as that shown in Fig. 1(b). Figure 1(b) reveals that in reality, the microstructures exhibit considerable disorder in the distribution of the fibrils and fiber bundles. Furthermore, the preform is seen to consist of capillary pathways of cross sectional sizes spanning several length scales ranging from nominal inter-fibril spacings within a fiber bundle (typically on the order of a micron) to representative inter-bundle distances (on the order of a fraction of a mm), at the upper end. As a result, the use of a single diameter capillary in the capillary-based permeability models is inappropriate.

It is evident from the foregoing discussion that a fundamental description of the disordered preform structures is of critical importance in the evaluation of the flow permeabilities, and forms the focus of this paper. The disordered nature of preform microstructures (Fig. 1(b)), coupled with the presence of multiple length scales for resin flow, suggests the existence of a fractal structure [20, 21] formed by the pores in the preform. This is supported by the observations reported in the literature on porous sedimentary rocks, which are fundamentally analogous in their microstructures to those of preforms used in liquid composite molding, and are shown to exhibit fractal pore networks for fluid flow [22, 23]. Fractal techniques have been used in diverse engineering applications that involve physical phenomena in disordered structures and over multiple scales [24–28]. In all these applications, the fractal dimensions have been very effective in rendering complex structures tractable for analysis, and it is this capability which is explored for describing the preform microstructures in the present context.

In this paper, the preform microstructures are characterized using two fractal dimensions [20, 21], one relating the size of the capillary pathways for resin flow to their population in the preform cross section, and the other describing the tortuosity (the extent of convolutedness) of the capillary pathways. The fractal description of the pore structures is used to construct a flow model which yields an analytical expression for the permeability in terms of the fiber volume fraction in the preform and the two fractal dimensions. A methodology for the evaluation of the fractal dimensions of actual microstructures is presented, along with experimental validation of the fractal permeation model for the case of knitted fiber preform architectures, over a wide range of processing conditions. A noteworthy distinction of the present work is that while fractal dimensions have been used in literature for characterizing material microstructures as an objective by itself (e.g., Ref. [24]), this paper presents a practical use of these geometric descriptors in the evaluation of a material parameter.

The organization of the paper is as follows: Section 2 provides a brief introduction to the principles of fractal geometry which will be used in the subsequent model development. Section 3 explains the fractal description of the preform pore structures and the governing equations, while a permeability model based on this description is presented in Section 4, and the methodology for the evaluation of the fractal dimensions is given in Section 5. The experimental studies aimed at validating the theoretical developments are discussed in Section 6, and the results of the study are presented in Section 7.

2. Fractal geometry

Euclidean geometry describes regular objects such as points, curves, surfaces, and cubes using integer dimensions 0, 1, 2, and 3, respectively. Associated with each dimension is a measure of the object such as the length of a line, area of a surface and volume of a cube. However, a multitude of natural objects and engineering constructs do not conform to an Euclidean description since their length, area and volume are scale-dependent [20]. Such objects are called fractals, and are described using a non-integral dimension called the fractal dimension [20, 21].

As an illustrative example, if one were to measure the length of a coastline of a country, the length would depend on the size of the measuring stick used; decreasing the length of the measuring stick leads to a better resolution of the convolutions of the coastline, and as the length of the stick approaches zero, the coastline's length approaches infinity. This is the fractal nature of the coastline. Owing to its convolutions, the coastline tends to fill space on a plane and its fractal dimension lies between the Euclidean dimension of a line, namely 1, and that of a plane, which has a value 2 [20]. The measure of a fractal structure, $M(L)$, the coast length in the above example,

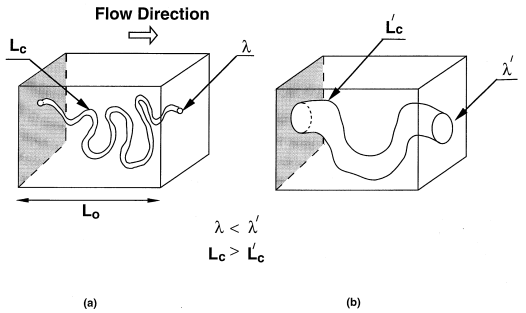

Fig. 2. Schematic of a representative preform volume composed of tortuous λ-sized capillaries. Sketches (a) and (b) illustrate the decrease in tortuosity with increasing capillary size.

is related to the length scale, L, through a scaling relationship of the form

$$M(L) \sim L^{d_f} \tag{1}$$

where '$\sim$' is read as 'scales as', and d_f is the fractal dimension of the structure.

Associated with equation (1) is the property of self-similarity, which implies that the value of d_f calculated from the relationship in Eq. (1) remains constant over a range of length scales, L. Geometric constructs such as the Sierpinsky gasket and the Koch curve are examples of exact fractals which exhibit identical self-similarity over an infinite range of length scales [20, 21]. However, self-similarity in a global sense is seldom observed in actual applications and the fractal description is based on a statistical self similarity, which the objects exhibit in some average sense, over a certain local range of length scales, L, relevant to the problem [27–30]. The associated statistical fractal dimension—referred to in this paper simply as the fractal dimension, for brevity—is usually estimated as the slope of a linear fit of data on a log–log plot of an average measure, $M(L)$, against the length scale, L. Further details on fractal geometry appear in publications by [20, 21, 30–33], which the interested reader is referred to.

The concept of local, statistical similarity introduced above is used in the following section to develop a geometric description of the preform pore structures.

3. Fractal description of preform pore structures

Consider a representative cubic preform volume of size L_o, as shown in Fig. 2. The preform volume can be envisioned to be made up of tortuous capillaries of various sizes ranging from nominal inter-fibril spacings at the lower end to typical inter-bundle separations at the upper end. Let the size of a generic capillary be λ, and its tortuous length within the preform volume be $L_c(\lambda)$, as illustrated schematically in Fig. 2(a). Owing to the tortuous nature of the capillary, its end-to-end length, $L_c(\lambda)$, is greater than the side of the cubic volume, L_o. Furthermore, the extent to which a capillary is convoluted within the preform volume, i.e., its tortuosity, depends on the capillary size, λ; the smaller the capillary size, greater is its tortuous length, and vice versa, as illustrated schematically in Fig. 2(a) and (b). Thus, the capillary exhibits a fractal tortuosity with respect to the capillary size, λ, and its length (expressed in a dimensionless form by scaling with respect to the cube dimension) is given by

$$\frac{L_c(\lambda)}{L_o} = \left(\frac{L_o}{\lambda}\right)^{d_T - 1}. \tag{2}$$

In Eq. (2), d_T is the fractal dimension of the capillary path, and lies in the range $1 < d_T < 2$. Higher values of d_T within this range correspond to a highly tortuous capillary, while $d_T = 1$ denotes a straight capillary path. The fractal dimension d_T pertains to the direction parallel to the flow path and the dimensionless capillary length, $L_c(\lambda)/L_o$, is also referred to as the capillary tortuosity, $T(\lambda)$. Note that the above equation reflects three important physical characteristics of the capillary tortuosity, that (1) it is always greater than or equal to unity, (2) it increases with decreasing λ, and (3) it is equal to unity for $\lambda = L_o$.

Eq. (2) describes the convolutedness of the capillary pathways and is one of the relationships characterizing the fractal pore structure. In order to describe the pore structure of the fibrous preform completely, it is also essential to determine the number of capillary pathways corresponding to every pore size, λ. This is obtained by considering a cross sectional plane of the preform volume normal to the overall flow direction, as shown by the shaded planes in Fig. 2(a) and (b). The capillary pathways intersecting the plane range in cross sectional sizes from a minimum value of $\lambda_{\min}$ to a maximum value of $\lambda_{\max}$. The population of the intersecting pores in the cross section exhibits the general trend that $N(L \geqslant \lambda)$, which denotes the total number of pores of size exceeding or equal to a value λ, increases as the pore size, λ, decreases. This scaling relationship of the cumulative pore population in a cross section may be expressed mathematically as

$$N(L \geqslant \lambda) = \left(\frac{\lambda_{\max}}{\lambda}\right)^{d_N} \tag{3}$$

where d_N, the pore area dimension, is the fractal dimension of the intersecting pore cross sections with a plane normal to the flow direction. Since d_N defines a fractal surface in a two-dimensional plane, its value lies in the range $1 < d_N < 2$. Eq. (3) suggests that when λ corresponds to the maximum pore size, $\lambda_{\max}$, the number of pores greater than or equal to it is one. Conversely, when λ corresponds to the smallest pore size, the number of pores

greater than $\lambda_{\min}$ is maximum. The above equation is analogous to the number–area relationship in the context of the geomorphology of the earth [20], for which the total number of islands of areas greater than a particular area, a, follows the power law $N(A > a) \sim a^{-D/2}$, where D is the fractal dimension of the surface.

The number of pores whose sizes fall within the infinitesimal range λ to $\lambda + \mathrm{d}\lambda$ is obtained by differentiating the cumulative pore size distribution, Eq. (3), with respect to λ, and the resulting expression may be written as

$$\mathrm{d}N = -d_N \frac{\mathrm{d}\left(\frac{\lambda}{\lambda_{\max}}\right)}{\left(\frac{\lambda}{\lambda_{\max}}\right)^{d_N+1}}. \tag{4}$$

Note that the negative sign in the above equation reflects a decrease in the pore population with increasing pore size. The number–size relationship given by Eq. (4), together with the tortuosity equation, equation (2), forms the basis for the development of the permeability model discussed below.

4. Fractal permeation model

Permeation of resin through the preform during the process principally depends upon the preform permeability, the driving pressure differential for the flow, and the fluid viscosity. The preform permeability, in turn, is a function of the preform geometry, namely the preform architecture, which is quantified in terms of two fractal dimensions d_T and d_N, and the fiber volume fraction, v_f. In this section, we seek to develop an analytical model relating the permeability to the three geometric preform parameters. The overall approach to the model development consists of (a) determining the total volumetric flow rate, Q, through the representative preform volume, and (b) using Darcy's law [16], to determine the effective permeability, κ.

For the purpose of the model development, the overall resin flow is considered to be in the direction as shown in Fig. 2(a). The corresponding permeability would be a component of the permeability tensor along the direction of flow. The other principal permeabilities may be evaluated following a similar procedure as that presented here. Since the flow of resin through the preform results from flow through several tortuous capillary pathways of various sizes as mentioned before, the overall volumetric flow rate, Q, through the preform shown in Fig. 2, is a cumulative of the flows through all the individual capillaries. Considering the tortuous flow through a single λ-sized capillary to be flow through an equivalent straight capillary of length, $L_c(\lambda)$, the flow rate, $q(\lambda)$, is given by the Hagen–Poiseulle equation [34],

$$q(\lambda) = g_q \frac{\Delta p}{L_c(\lambda)} \frac{\lambda^4}{\mu} \tag{5}$$

where Δp is the pressure differential applied to drive the flow, μ is the viscosity of the resin permeating through the preform, and g_q is a geometric factor based on the shape of the capillary cross section (for a circular cross section, $g_q = \pi/128$, with λ as the cross sectional diameter), and L_c is the tortuous length of the capillary pathway, given by Eq. (2). Note that thermosetting resins used in the fabrication processes typically exhibit Newtonian rheology, for which the above equation is appropriate. However, if the permeant were a non-Newtonian fluid, Eq. (5) must be replaced by a suitable flowrate–pressure difference relationship, although the methodology presented below remains the same.

The net flowrate through all the capillaries whose cross-sectional size lie in the interval λ to $\lambda + \mathrm{d}\lambda$ is given by the product of the number of such capillaries, $\mathrm{d}N(\lambda)$ (Eq. (4)), and the individual capillary flowrate, $q(\lambda)$ (Eq. (5)). Further, the total volumetric flowrate, Q, through the representative preform volume is obtained by integrating the flowrate contribution by the pores in every $\mathrm{d}\lambda$ interval, over the entire range of prevalent pore sizes, $\lambda_{\min}$ to $\lambda_{\max}$ in the preform. The resulting expression for Q is as follows

$$\begin{aligned} Q &= \int_{\lambda_{\min}}^{\lambda_{\max}} q(\lambda)\, \mathrm{d}N(\lambda) \\ &= g_q \frac{\Delta p}{\mu} \lambda_{\max}^3 \beta^{d_T} \left[1 + d_N \frac{(1-\alpha^{3+d_T-d_N})}{3+d_T-d_N} \right] \end{aligned} \tag{6}$$

where β is the maximum pore size, $\lambda_{\max}$, scaled with respect to L_o, and α is the minimum to maximum pore size ratio, $\lambda_{\min}/\lambda_{\max}$. The preform permeability, κ, is determined from the flow rate, Q, and using Darcy's law as

$$\kappa = \frac{\mu L_o Q}{\Delta p A_o} = g_q \lambda_{\max}^2 \beta^{1+d_T} \left[1 + d_N \frac{(1-\alpha^{3+d_T-d_N})}{3+d_T-d_N} \right]. \tag{7}$$

In the above equation, A_o $(= L_o^2)$, is the cross-sectional area of the representative preform volume normal to the overall flow direction. Note that the permeability is a function of only the geometrical parameters of the microstructure, namely α, β, and $\lambda_{\max}$, and the two fractal dimensions, d_T and d_N. The determination of these parameters is discussed in the remainder of this section.

4.1. Evaluation of α and β

The dimensionless parameters α and β appearing in the permeability expression (Eq. (7)) are determined from consideration of the overall pore volume fraction in the preform, which may be evaluated as the cumulative area fraction of the pores in a preform cross section. Since the pore distributions are statistically invariant from one preform cross section to another, the area fraction forms an accurate estimate of the volume fraction. The total

pore area in a cross section of the representative preform volume is determined following the steps used to arrive at the total flow rate, Q, above. The pore volume fraction, v_p, which equals $1-v_f$, where v_f is the fiber volume fraction in the preform, is then given by the ratio of the cumulative pore area to the cross sectional area, L^2_o, of the representative preform volume, i.e.,

$$v_p = 1-v_f = \frac{1}{L_o^2}\int_{\lambda_{\min}}^{\lambda_{\max}} g_v\lambda^2\,\mathrm{d}N(\lambda) = g_v\beta^2\left[1+d_N\left(\frac{1-\alpha^{2-d_N}}{2-d_N}\right)\right] \quad (8)$$

where g_v is a geometric factor for the pore area based on the pore cross sectional shape (e.g., $g_v = \pi/4$ corresponds to a circular pore cross section, with λ as the cross-sectional diameter).

As α approaches zero, the situation wherein the size of the smallest pores is negligible or the maximum pore is very large, the pore volume fraction in the preform, v_p, approaches the maximum achievable value of g_v.[1] Using this condition in Eq. (8) yields the following expression for β in terms of the fractal dimension d_N

$$\beta = \sqrt{\left(\frac{2-d_N}{2}\right)}. \quad (9)$$

Eq. (8) can now be rewritten as given below to obtain α as a function of the fiber volume fraction and the fractal dimension, d_N, by substituting for β from the foregoing equation.

$$\alpha = \left[\frac{2}{d_N}\left(1-\frac{1-v_f}{g_v}\right)\right]^{\frac{1}{2-d_N}} \quad (10)$$

4.2. Evaluation of λ_{max}

The maximum pore size, $\lambda_{\max}$, in the permeability expression (Eq. (7)) corresponds to the pore space formed between fiber bundles in the preform. The inter-bundle spaces are a function of the architectural parameters of the fiber mats, such as the weave type, the number of fiber bundles per unit length, and the bundle dimensions, as well as the number of layers of the fiber mats stacked inside the thickness of the mold cavity. The architectural parameters are specified by the manufacturer of the fiber mats, while the number of layers in the preform is decided based on the desired fiber volume fraction in the composite. The maximum pore size, $\lambda_{\max}$, can therefore be related to these known parameters.

The application of the fractal pore description and the permeation model are illustrated in this paper in the context of preforms made of a stack of knitted fiber mats. The knitted fabric architecture considered in the study consists of a layer of (ideally) equispaced, aligned fiber bundles knit to an identical layer of cross-running fiber bundles, resulting in a geometrically isotropic configuration. For this architecture, the maximum pore space (and therefore, $\lambda_{\max}$) may be considered to result from one of two ordered bundle arrangements in the preform, as explained below. When the number of fiber mat layers stacked inside the mold cavity is the minimum required to completely fill the mold cavity thickness, the preform cross section is likely to exhibit an in-line arrangement of the bundles within and across fiber layers. In this configuration, the centers of the bundles nominally form the vertices of a periodic rectangular unit cell, as shown in Fig. 3(a). On the other hand, for higher fiber volume fractions, which require a dense stacking of the fiber mat layers within the mold cavity, a staggered arrangement of the bundles with respect to bundles in adjacent fiber layers results, owing to the relative rearrangement of the bundles to accommodate the extra fiber mat layers. In such an arrangement the lines connecting the bundle centers nominally form a repeating triangular unit cell, as illustrated in Fig. 3(b).

The maximum pore area, $A_{p,\max}$, in each of these cases is the difference between the (rectangular or triangular) unit cell area, and the total bundle area enclosed within the unit cell, identified by the lightly-shaded regions in Fig. 3(a) and (b). The width of the unit cell, w, may be calculated using the information on the number of bundles per unit length in the fiber mats, while the unit cell height, h, is estimated as the ratio of the mold cavity thickness to the number of fiber mat layers, N, stacked in the mold cavity. Further, the fiber bundle area is determined assuming a lenticular shape for the bundle cross section. The resulting expressions for the maximum pore areas are given in Fig. 3, in terms of the known geometric parameters—a and b, which define the fibre bundle geometry, and w and h. The maximum pore size, $\lambda_{\max}$, is then given by $\lambda_{\max} = \sqrt{A_{p,\max}/g_v}$. Introducing the expressions for α, β, and $\lambda_{\max}$ in Eq. (7), the permeability emerges as a function of the fiber volume fraction, v_f, the architectural parameters of the fiber mats, and the fractal dimensions, d_T and d_N.

4.3. Evaluation of d_T and d_N

The fractal dimensions, d_T, and d_N, characterizing the preform pore structures are obtained from an analysis of representative microstructural images of the preform. The procedure for the calculation of d_T and d_N, for a given microstructural image, is presented below, while the practical implementation details related to the image acquisition and analysis are described later in this article, under Experimental Studies.

[1] The reader may verify this by considering a Sierpinsky carpet [21] in the limit of the number of generations approaching ∞.

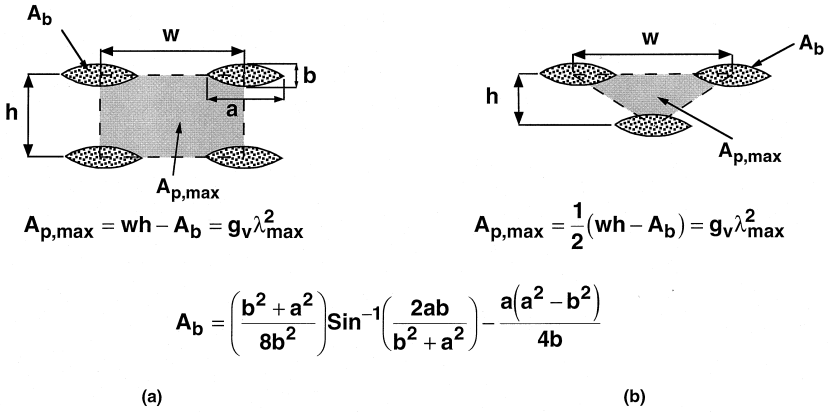

Fig. 3. Illustration of the (a) rectangular, and (b) staggered arrangements of the fiber bundles considered in the estimation of the maximum pore size, λ_{max}.

4.3.1. Tortuosity dimension, d_T

As mentioned previously, the tortuosity dimension, d_T, represents the extent of convolutedness of the capillary pathways for resin flow through the preform. Since the tortuosity dimension pertains to the capillary pathways in the direction of the overall resin flow, or equivalently the principal direction for the permeability evaluation, the microstructural images considered for the calculation of d_T are those of the preform cross section parallel to the flow direction. Further, since the tortuosity of the flow pathways results from the convolutions of the boundaries of the porous regions as seen in a two-dimensional preform cross section (equivalently, the surface of the porous pathways in a three-dimensional volume), the tortuosity dimension, d_T, may therefore be evaluated as the fractal dimension of the *perimeter* of the porous regions. It may be readily seen that the perimeter fractal dimension—as also the tortuosity dimension—for a preform consisting of straight capillary pathways is unity, and conversely, perimeter fractal dimension, and tortuosity dimension values approaching 2 are associated with highly convoluted capillaries that tend to fill a two-dimensional plane completely (analogous to the example of the coastline presented in an earlier section).

The tortuosity dimension may be obtained using the box counting method [20, 21] applied to the perimeter of the porous regions in the preform microstructures. In this method, the cross section under analysis is discretized using square boxes of size, L, and the number of such L-sized boxes tracing the perimeter of the pore regions is recorded as $N(L)$. This step is repeated for various box sizes, and a log–log plot of $N(L)$ against L is constructed. The magnitude of the slope of a best-fit straight line through the data yields the tortuosity dimension, d_T.

Figure 4(a) shows a typical preform microstructure, wherein the black regions represent the fibers, and the remaining areas denote the pores. Figure 4(b) presents example data obtained from the box-counting method applied to the pore boundaries in the microstructure over the length scale range $2 \leqslant L \leqslant 16$ pixels. It may be noted from Fig. 4(b) that, as expected, the number of boxes required to cover the perimeter decreases with increasing box size. Furthermore, the data points closely follow a straight line, which confirms the fractal nature of the microstructure.

4.3.2. Area dimension, d_N

The evaluation of the area dimension is based on the analysis of a representative cross section of the microstructure along a plane normal to the principal direction of resin flow. The area dimension may be obtained from one of two methods: (a) the 'sandbox method' [31] and (b) the box-counting method [20, 21]. Although both these methods yield similar estimates of the fractal dimensions [35], the box-counting method is computationally faster, and was used in this study. The procedure remains similar to that described above for the determination of the tortuosity dimension, with the only difference that $N(L)$ now pertains to the number of boxes required to completely cover the pore areas. As before, the area dimension, d_N, is determined as the magnitude of the slope of a linear fit through data on a log–log plot of $N(L)$ vs L. Figure 4(c) shows the data obtained from the box-counting method applied to pore areas in the microstructure in Fig. 4(a) over the length scale range $2 \leqslant L \leqslant 16$ pixels. The high degree of linear correlation of the data, similar to that seen in Fig. 4(b), additionally proves the existence of fractal pore structures in the preform.

5. Experimental studies

Experimental studies were carried out with the objectives of (a) investigating the effects of the process and

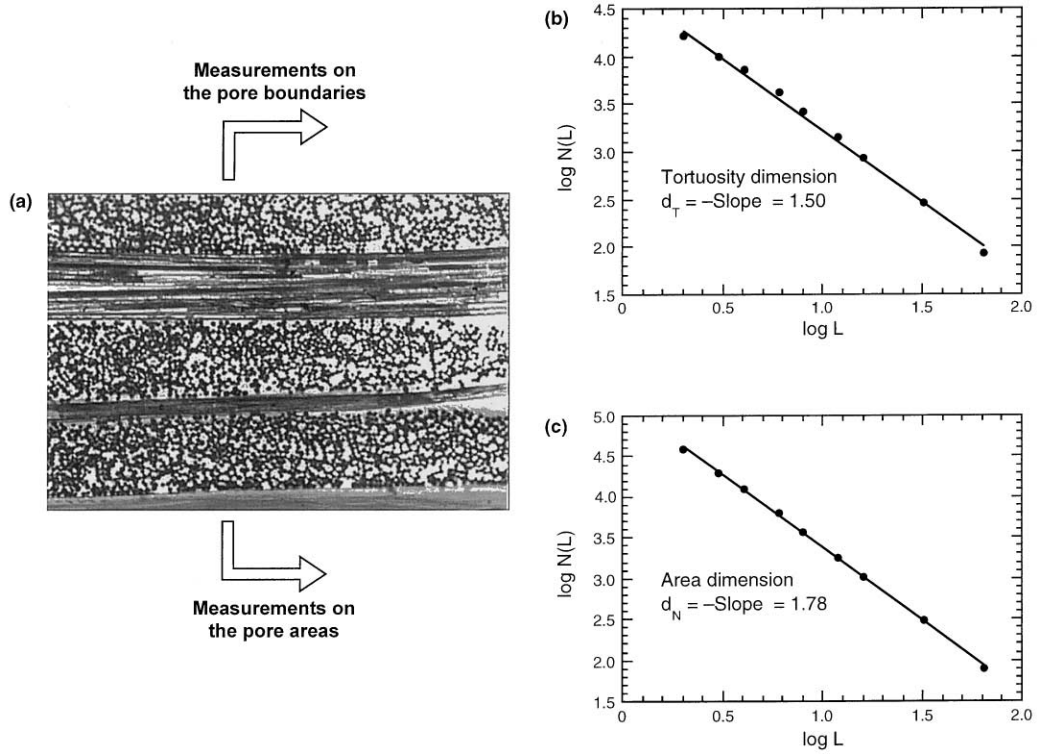

Fig. 4. Schematic illustration of the procedure for evaluation of the tortuosity dimension, d_T (b), and the area dimension, d_N (c) for the sample preform microstructure shown in (a).

material parameters on the permeability of preforms for an actual resin and catalyst system, and (b) validating the theoretical permeability model developed in the foregoing section. The experimental studies were conducted using a lab-scale resin transfer molding (RTM) facility described below. Note that since the fundamental flow characteristics in resin transfer molding are the same as those in other infiltration-based processing techniques, the studies presented herein bear a broader significance. The resin transfer molding process is attractive from the viewpoint of experimental investigations owing to its low pressure requirements.

The main components of the experimental setup, shown schematically in Fig. 5, include a pressure tank containing the catalyzed resin, and a mold in which the preform is placed. The mold is constructed as a sandwich of three layers—a bottom aluminum base plate, a middle Plexiglas spacer, and a top Plexiglas plate. The aluminum base plate comprises of a 1/4 in. diameter resin inlet port that discharges into a concave runner along the width of the mold, as illustrated in Fig. 5. The runner ensures an uniform, essentially one-dimensional permeation of the preform along the mold length. The base plate additionally incorporates a cavity that houses a 9 W/in^2 strip heater adhesively bonded to the bottom of a copper plate, and backed by fibreglass insulation layers. The copper

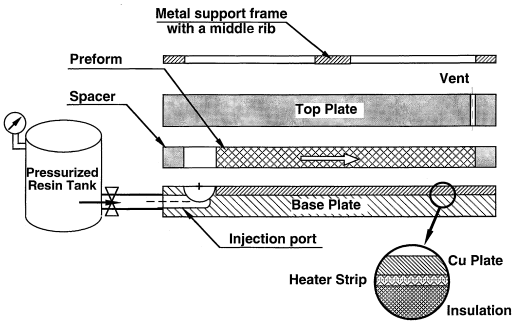

Fig. 5. Experimental setup used for the permeation studies.

plate ensures uniform surface heating of the composite during the cure process, and has five embedded thermocouples for temperature measurement and heater control. The top surface of the copper plate was ground to a smooth finish in order to minimize the surface interaction with the resin flow, and was mounted flush with the surface of the aluminum base plate.

The middle spacer, placed between the base plate and the Plexiglas top plate, determines the size of the mold cavity which was kept constant in this study at $6 \times 3 \times 0.125$ in. The transparent top plate, made of 0.5

in. thick Plexiglas, consists of two air vents drilled to be in-line with the far corners of the mold cavity along the edge away from the injection face, as shown in Fig. 5. An aluminum frame of the same dimensions as the spacer, but with a 0.5 in. wide mid-rib as shown in Fig. 5, was placed above the top plate and served to (a) distribute the clamping force evenly on the mold, and (b) prevent any deformation of the top plate due to the injection pressures. The overall sandwich setup was secured by six hexagonal bolts.

The porous preforms used in the permeation studies were made by stacking layers of knitted glass fabric characterized by an isotropic fiber architecture in the fabric plane (Model A1110, Collins Craft Company). The experiments were conducted using an epoxy resin, EPON-815 catalyzed with EPICURE 3274, both supplied by the Shell Chemical Company. The resin selection was based on its low viscosity which permitted investigation of a wide range of fiber volume fractions using relatively low injection pressures. The use of an actual resin system for the permeability measurements is a noteworthy distinction of the present studies vis-à-vis those in the literature based on simulated fluids such as corn syrup and motor oil, among others. All the experiments were conducted at isothermal conditions, wherein the resin and the preform were at room temperature throughout the injection process.

For each combination of the preform fiber volume fraction and resin injection pressure, the permeation rate was measured by timing the flow of the resin as it exited through the two vents into a collection beaker. The preform permeabilities were then calculated from Darcy's law using the measured flow rates, the pressure gradient over the mold length, and the preform cross sectional area. Permeability measurements were obtained for injection pressures ranging from 12 psi for a fiber volume fraction of 38% to 75 psi for the 58% fiber volume fraction. The permeability data was used in the model validation discussed in the next section.

5.1. Image analysis

Apart from providing the permeability data representative of those encountered in realistic processing environments, the use of a catalyzed resin in the experiments also provided for preserving the relative fiber arrangement in the preform for calculation of the two fractal dimensions, d_T and d_N, using image analysis. A consequence of the isotropic fabric architecture used in the study is that the preform cross sections are nominally identical along the planes normal to, and parallel to the principal flow direction. This simplifies the image analysis procedure, wherein the same cross section may be used for obtaining both the fractal dimensions.

Specimens were cut along the width of the rectangular plate samples fabricated, which provided for analysis of the microstructures on planes normal to the flow direction. The samples were mounted in a quick-setting epoxy and polished to a fine finish for optical inspection. Further, in order to obtain enhanced contrast between the glass fibers and the epoxy matrix during image analysis, since both exhibit similar optical transparency, the glass fibers were etched using a 20% hydrofluoric acid solution.

The polished specimens were analyzed under a Nikon Optiphot optical microscope at a magnification of $10\times$, by considering four adjacent fields of view on the microstructure. This ensured analysis of the complete spectrum of features ranging from the inter-fibril to the inter-bundle scales. Using a transmitted light source, the representative sections of the microstructure were captured via a Scion image grabber into a Power PC Macintosh computer (8100/100AV), from a Hitachi CCD camera mounted on the microscope. The fractal dimensions of the captured digitized images were obtained using the box-counting method described previously, which was implemented in the image analysis software NIH Image (available from the National Institute of Health). The fractal dimensions, d_T and d_N, were used in the theoretical model (Eq. (7)) to evaluate the permeabilities.

6. Results and discussion

The results presented in this section are aimed at (a) demonstrating the fractal characteristics of actual pore structures, (b) illustrating the parametric effects of the two fractal dimensions on the permeabilities, and (c) providing experimental validation of the theoretical model.

It may be recalled that the fractal permeation model was founded upon a fundamental relationship between the cumulative pore count and the pore area, given by Eq. (3). The existence of this scaling relationship in actual microstructures is demonstrated in Fig. 6, wherein the

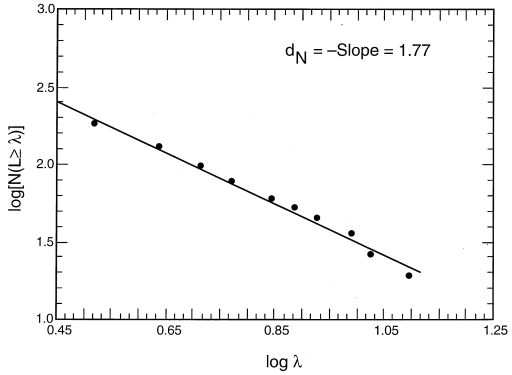

Fig. 6. Plot of the cumulative pore count, $N(L \geqslant \lambda)$, as a function of the pore size, λ, for the example microstructure in Fig. 4(a).

data correspond to measurements on the micrograph of a preform with a 38% fiber content by volume, shown in Fig. 4(a). The figure shows a log–log plot of the cumulative number of pores, $N(L \geqslant \lambda)$, whose cross-sectional sizes (given by the square-root of the cross-sectional area) exceed a value λ, as a function of the pore size, λ. It is seen that the cumulative pore count decreases as the pore size increases, as implied by Eq. (3). Furthermore, the measurements follow a linear variation on a logarithmic scale, which together with the data presented in Fig. 4(b) and (c), confirms the statistical fractal nature of the microstructures. It is evident from Fig. 6 that a larger value of d_N corresponds to a sharp increase in the number of the smaller pores relative to the larger pores. Also noteworthy is the fact that the area dimension, d_N, obtained from the cumulative pore count data matches closely with the result of the box-counting method in Fig. 4(c).

The parametric effects of the area dimension, d_N, the tortuosity dimension, d_T, and the fiber volume fraction, v_f, on the model-predicted permeabilities, κ, are plotted in Fig. 7(a) and (b). Fig. 7(a) shows the permeability variation with the area dimension, d_N, for different values of the tortuosity dimension, and a fixed fiber volume fraction of 0.48. It is seen that the permeability decreases as d_N and d_T increase. The decrease in permeability with the increase in d_T is attributed to the increased flow resistance due to the highly-convoluted capillary pathways. An increase in d_N corresponds to a decrease in the number of the larger pores, and an increase in the population of smaller pores within a representative preform volume. The resulting reduction in the available area for resin flow in turn leads to a decrease in the permeability. An interesting fact elucidated in Fig. 7(a) is that for any tortuosity dimension, as the area dimension, d_N, approaches its largest possible value of 2, the permeability approaches zero. This theoretical limit on d_N corresponds to the situation wherein the preform predominantly consists of pores of sizes approaching zero, which no longer contribute to the resin flow.

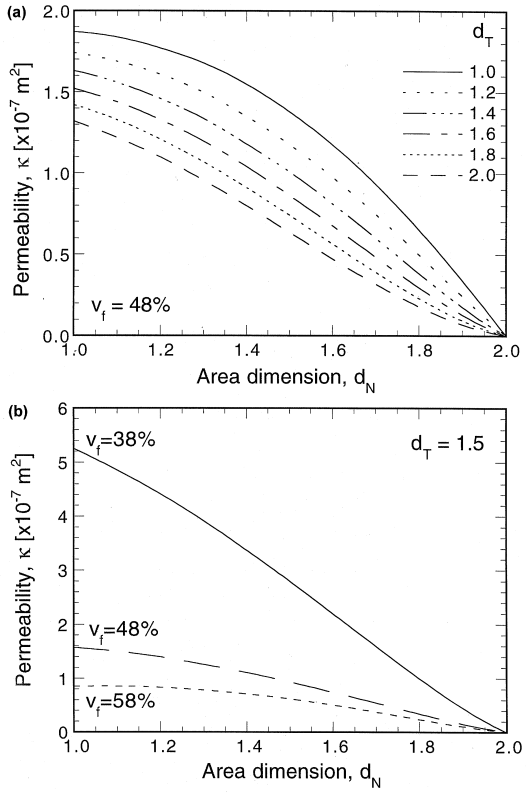

Fig. 7. Parametric effects on the model-predicted permeability: (a) influence of the fractal dimensions, d_T and d_N, for a fiber volume fraction of 48%, and (b) effects of the fiber volume fraction, v_f, and the area dimension, d_N, for a tortuosity dimension, d_T, of 1.5.

The variation of the preform permeability with the fiber volume fraction, v_f, and the area dimension, d_N, is presented in Fig. 7(b). The results shown correspond to the tortuosity dimension being held constant at 1.5. The permeability is seen to decrease with increasing area dimension, as also observed in Fig. 7(a). Furthermore, the permeability decreases with increasing fiber volume fraction in the preform owing to the reduction in the available pore volume for the resin to permeate through.

As described in the previous section, experimental studies were conducted towards validating the theoretical model. The investigations considered preform fiber volume fractions of 0.38, 0.48, and 0.58, with four different injection pressures for each fiber volume fraction. The fractal dimensions, d_N and d_T, were evaluated for each of the 12 cases using the procedure outlined previously. The maximum pore size, λ_{max}, was calculated for each fiber volume fraction as described in Fig. 3. The architectural parameters (such as the bundle width, the inter-bundle spacing, and the fiber mat thickness) for the knitted glass fabric reinforcements, needed in the calculations, were obtained from the materials supplier, and independently verified with measurements on the fabric mats. The values of λ_{max} were calculated to be 1.03, 0.60, and 0.50 mm, respectively, for the three fiber volume fractions of 0.38, 0.48 and 0.58. These analytical estimates were confirmed to be in close agreement with the maximum pore sizes of 0.98, 0.63, and 0.55 mm, measured on actual microstructures, for the three volume fractions. Furthermore, the geometric factors, g_q and g_v, appearing in the permeability model, were taken to be unity. The results of the experimental investigations are presented in Figs 8 and 9 as described below.

Fig. 8 presents the variations of the tortuosity dimension (solid lines) and the area dimension (dashed lines) with the injection pressure and the fiber volume fraction. It is seen that, in general, both the fractal dimensions decrease with increasing injection pressure. This may be

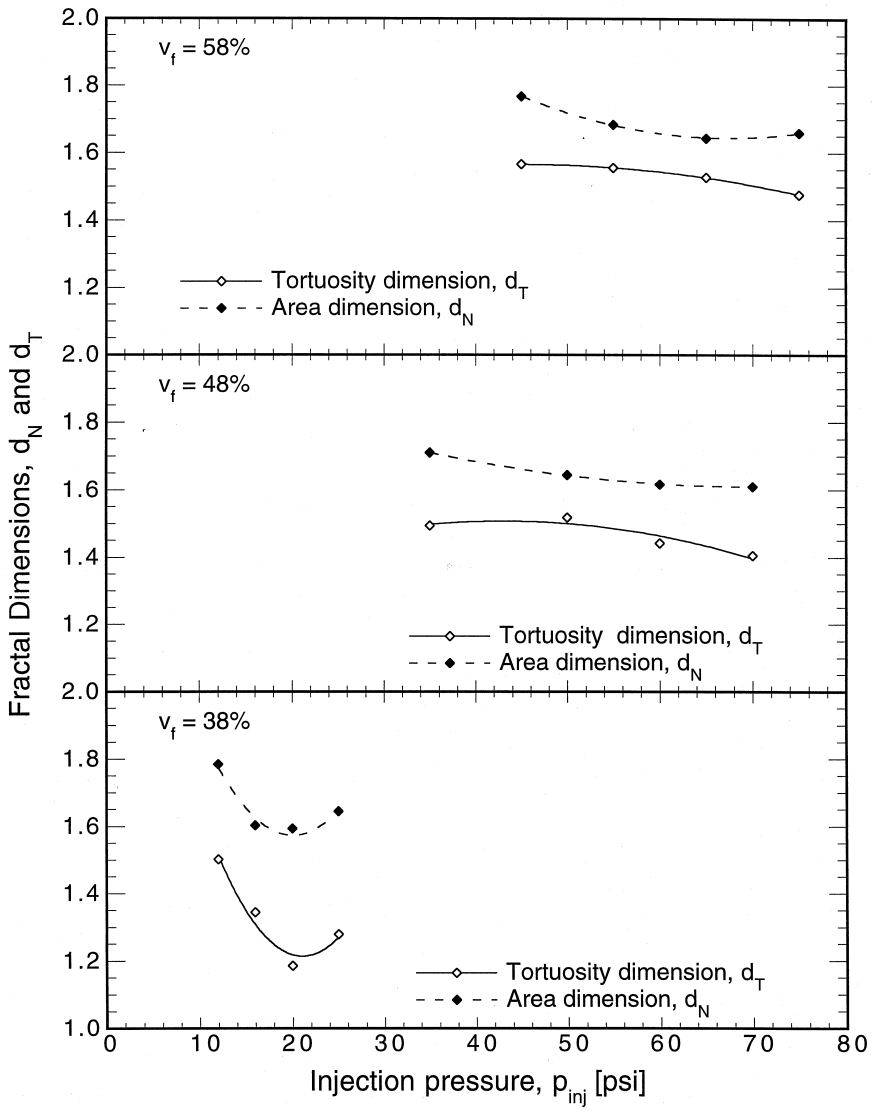

Fig. 8. Variation of the measured fractal dimensions, d_T and d_N, with injection pressure, p_{inj}, for the three fiber volume fractions studied.

attributed to the dilation of the pores in the preform resulting from a microstructural rearrangement, for a constant pore volume fraction, induced by the higher fluid pressures. In particular, the decrease in the area dimension with injection pressure suggests a dilation of the smaller pores rather than the larger ones. The increased pore size in turn leads to reduction in the tortuosity dimension of the flow pathways and therefore, a decrease in the tortuosity dimension. Furthermore, for a fixed injection pressure, both the tortuosity dimension and the area dimension are seen to increase with increasing fiber volume fraction. For example, at an injection pressure of 60 psi, the tortuosity dimension increases from 1.45 for $v_f = 48\%$ to 1.55 for $v_f = 58\%$, and the corresponding area dimension increase is noted to be from 1.60 to 1.65 (Fig. 8). The tighter packing of the fiber mats at the higher volume fractions leads to the resin flow taking on a more tortuous path which is reflected in the increased tortuosity dimension values. Moreover, the dense fiber packing causes a skew in the pore size distribution towards the smaller values, resulting in an increase in the area dimension, d_N.

The variation of the experimentally-measured and the model-predicted permeabilities with the injection press-

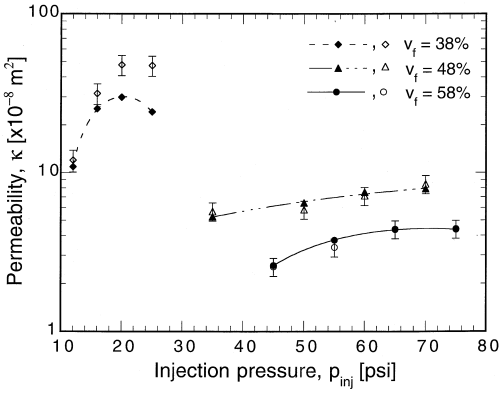

Fig. 9. Comparison of the model-predicted permeabilities with experimental data, for all the cases studied.

ure for the three different fiber volume fractions studied is plotted in Fig. 9. The solid symbols in the plot represent the model-predicted values, while the experimental data are denoted by open symbols. The lines connecting the solid symbols represent curve fits through the model predictions and serve to elucidate the general trend in the permeability variation. The error bands on the experimental data vary from 14% for the 0.38 fiber volume fraction runs, to 12% for the 0.58 fiber volume fraction cases.

Fig. 9 shows that the permeability increases with the injection pressure—a trend also reported by Karbhari et al. [10]. This trend closely correlates to the decrease in the fractal dimensions with increasing injection pressure seen in Fig. 8, and is attributed to the dilation of the pores in the preform due to increased fluid pressure. The dilated pores in turn lead to a reduced flow resistance and therefore, an increase in the permeability. For the higher fiber volume fractions, owing to the tighter stacking of the fiber mats, the pore dilation effect and the permeability increase with injection pressure are seen to be less pronounced. Fig. 9 also demonstrates a decrease in the permeability with increasing fiber volume fraction, which as mentioned previously is due to the reduction in the available flow volume for the resin. Furthermore, the increase in the capillary tortuosity with increasing fiber volume fraction noted in Fig. 8, additionally contributes to the enhanced flow resistance, and the decrease in the preform permeability.

Fig. 9 reveals an excellent agreement between the model predictions and the experimental data over the range of parameters studied. Especially noteworthy is the fact that the model correctly predicts the increasing trend in permeability with injection pressure. By way of contrast, the available theoretical models do not reflect the pressure-dependence of the permeability. In almost all the cases, the agreement is to within about 10%. For the higher injection pressures in the case of $v_f = 38\%$, although the model estimates an increase in the permeability, the predicted values are lower than the experimental measurements. A possible cause for this is the relative displacement of the loosely-packed fiber mats during the resin injection process thereby resulting in preferential flow paths of reduced resistance and higher permeabilities.

The foregoing results demonstrate the effectiveness of the fractal permeation model in evaluating the permeabilities of practical microstructures. The remarkable validation with experimental measurements is particularly significant in light of the fact that unlike the models reported previously in the literature which include empirical constants, the parameters of the present model are all uniquely determined based on the actual microstructural information. Further, from a fundamental viewpoint, this article presented the use of fractal techniques in a predictive paradigm toward evaluating a property of practical interest, rather than as a solely descriptive tool. Nondestructive means of evaluating the fractal dimensions of the preform microstructures inside the mold prior to infiltration are presently being investigated, which will render the model a valuable tool for process modeling and on-line model-predictive process control applications. These developments will be reported in the future.

The present study focused on the development of the permeation model and illustrated the predictive capabilities of the model in the context of preforms made of knitted fiber architectures that are isotropic in the fabric plane. The use of the model for other preform architectures as well as for anisotropic configurations is described elsewhere [35], which the interested reader is referred to. The methodology presented in this article may be applied to describing the permeability of porous media encountered in other application areas as well.

7. Conclusions

A novel approach using the tool of fractal dimensions was presented for description of the disordered pore structures of preforms used in liquid composite molding processes. The fractal pore description was used to obtain an analytical expression for the permeabilities of the preform. Experimental validation of the fractal model was conducted over a wide range of injection pressures and fiber volume fractions. Excellent agreement was demonstrated between the predicted and the measured permeability values. The theoretical model was also shown to describe detailed effects such as the pressure-dependence of the permeability accurately.

Acknowledgements

The authors gratefully acknowledge the financial support provided by the National Science Foundation (Grant No. DMI-9522801), and the Office of Naval Research through a Young Investigator Award (Contract No. N00014–96-1-0726) with Mr James J. Kelly as the Scientific Officer. The authors also wish to thank the Collins Craft Company and the Shell Chemical Company for providing gratis the materials used in the study.

References

[1] C.F. Johnson, Resin transfer molding, in: Engineered Materials Handbook, Vol. 1: Composites, ASM International, Metals Park, OH, 1987, pp. 564–568.
[2] M. Valenti, Resin transfer molding speed composite making, Mechanical Engineering 114 (11) (1992) 46–48.
[3] S.G. Advani, M.V. Bruschke, R.S. Parnas, Resin transfer molding transfer phenomena in polymeric composites, Vol. 10, in: S.G. Advani (Ed.), Flow and Rheology in Polymer Composites Manufacturing, Elsevier Science, The Netherlands, 1994, pp. 465–515.
[4] M.V. Bruschke, S.G. Advani, A numerical simulation of resin transfer mold filling process, in: Proceedings of ANTEC '89, 1989, pp. 1769–1773.
[5] S.I. Guceri TGMOLD: A Molding Simulation Code, User's Manual, Department of Mechanical Engineering, University of Delaware.
[6] R. Dave, A unified approach to modeling resin flow during composite processing, Journal of Composite Materials 24 (1990) 22–41.
[7] Y.R. Kim, S.P. McCarthy, J.P. Fanucci, S.C. Nolet, C. Koppernaes, Resin flow through fiber reinforcements during composites processing, SAMPE Quarterly (1991) 16–22.
[8] R.S. Parnas, F.R. Phelan, The effects of heterogeneities in resin transfer molding preforms on mold filling, in: Proceedings of the 36th International SAMPE Symposium, 1991, pp. 506–519.
[9] B.T. Astrom, R.B. Pipes, S.G. Advani, On flow through aligned fiber beds and its applications to composites processing, Journal of Composite Materials 26 (9) (1992) 1351–1373.
[10] V.M. Karbhari, D.A. Steenkamer, G.R. Palmese, Effect of preform architecture on flow and processing in resin transfer molding. SAE Technical Paper 930166, Presented at the SAE International Congress and Exposition, 1993.
[11] Z. Cai, C. Berdichevsky, An improved self-consistent method for estimating the permeability of a fiber assembly, Polymer Composites 14 (4) (1993) 314–323.
[12] R.J. Lin, L.J. Lee, M.J. Liou, Mold filling and curing analysis in liquid composite molding, Polymer Composites 14 (1) (1993) 71–81.
[13] S. Ranganathan, S.G. Advani, G.M. Wise, F.R. Phelan, R.S. Parnas, A numerical and experimental study of the permeability of fiber preforms, in: Proceedings of the 10th Annual ASM/ESD Advanced Composites Conference, Dearborn, MI, 1994, pp. 309–319.
[14] Jvd Westhuizen, J.P. Du Plessis, Quantification of unidirectional fiber bed permeability, Journal of Composite Materials 28 (1994) 619–637.
[15] H. Darcy, in: Les fontaines publiques de la ville de Dijon, Dalmont, Paris, 1856.
[16] J. Happel, H. Brenner, in: Low Reynolds Number Hydrodynamics, Mechanics of Fluids and Transport Process, Martinus Nejhoff, Boston, 1986.
[17] J. Kozeny, Wiss, Sitzungsber, Weiner Akad IIa (1927) 136.
[18] J. Happel, Viscous flow relative to arrays of cylinders, AIChE Journal 5 (2) (1959) 174.
[19] A.S. Sangani, A. Acrivos, Slow flow past periodic arrays of cylinders with application to heat transfer, International Journal of Multiphase Flow 8 (3) (1982) 193–201.
[20] B.B. Mandelbrot, in: The Fractal Geometry of Nature, W. H. Freeman, New York, 1983.
[21] J. Feder, in: Fractals, Plenum Press, New York, 1988.
[22] R.R. Nigmatullin, L.A. Dissado, N.N. Soutougin, A fractal pore model for Archie's law in sedimentary rocks, Journal of Physics, D: Applied Physics 25 (1992) 32–37.
[23] A.J. Katz, A.H. Thompson, Fractal sandstone pores: Implications for conductivity and pore formation, Physical Review Letters 54 (1985) 1325–1328.
[24] K. Kindo, et al., High magnetic field effect in martensite transformation, Physica B 155 (1989) 207–210.
[25] A. Majumdar, C.L. Tien, Fractal network model for contact conductance. ASME Paper 89-HT-20, 1989.
[26] P. Maragos, F.K. Sun, Measuring the fractal dimension of signals: Morphological covers and iterative optimization. Technical Report, CICS-P-193, Center for Intelligent Control Systems, M.I.T., Cambridge, MA 02139, 1990.
[27] R. Pitchumani, S.C. Yao, Correlation of thermal conductivities of unidirectional fibrous composites using local fractal techniques, Trans. ASME, Journal of Heat Transfer 113 (4) (1991) 788–796.
[28] R. Pitchumani, A fractal geometry approach to modeling disordered composite microstructures and their properties, in: T.W. Chou, J. Vinson (Eds.), Proceedings of the Ninth Technical Conference of the American Society for Composites, Technomic Publishing Company, 1994, pp. 809–819.
[29] C.A. Pickover, A. Khorasani, On the fractal structure of speech waveforms and other sampled data, Research Report No. 11305. Computer Science Department, IBM Thomas J Watson Research Center, Yorktown Heights, NY 10598,1985.
[30] R.F. Voss, Random fractals: Characterization and measurement, in: R, Pynn, A. Skjeltorp (Eds.), Scaling Phenomena in Disordered Systems, 133, NATO ASI Series B, Plenum, New York, 1985, pp. 1–11.
[31] H.E. Stanley, et al., Applications of scaling and disorderly growth phenomena to oil recovery, in: R. Pynn, A. Skjeltorp (Eds.), Scaling Phenomena in Disordered Systems, 133, NATO ASI Series B, Plenum, New York, 1985, pp. 85–97.
[32] H.E. Stanley, Fractal concepts for disordered systems: the interplay of physics and geometry, in: R. Pynn, A. Skjeltorp (Eds.), Scaling Phenomena in Disordered Systems, 133,

NATO ASI Series B, Plenum, New York, 1985, pp. 49–69.

[33] H.E. Stanley, N. Ostrowsky, in: On Growth and Form. Fractal and Non-fractal Patterns in Physics, NATO ASI Series, Series E: Applied Sciences, No. 100, Martinus Nejhoff, Dordrecht, Netherlands, 1986.

[34] M.M. Denn, in: Process Fluid Mechanics, Prentice-Hall, NJ, 1980.

[35] B. Ramakrishnan, R. Pitchumani, Fractal permeation characteristics of preforms used in liquid composite molding, Polymer Science and Engineering (1998) (submitted).